

We are IntechOpen, the world's leading publisher of Open Access books Built by scientists, for scientists

6,900

Open access books available

186,000

International authors and editors

200M

Downloads

Our authors are among the

154

Countries delivered to

TOP 1%

most cited scientists

12.2%

Contributors from top 500 universities



WEB OF SCIENCE™

Selection of our books indexed in the Book Citation Index
in Web of Science™ Core Collection (BKCI)

Interested in publishing with us?
Contact book.department@intechopen.com

Numbers displayed above are based on latest data collected.
For more information visit www.intechopen.com



Multiscale Micro/Nanostructured Heat Spreaders for Thermal Management of Power Electronics

Huihe Qiu and Yinchuang Yang

Abstract

In this chapter, we describe surface modification techniques for enhancing heat/mass transfer and evaporation on heated surfaces. The effect of asymmetrical structure in designing a vapor chamber, patterned with multiscale micro/nanostructured surfaces will be introduced. The wettability patterned surface and its mechanism for improving the evaporation rate of a droplet and the thermal performance of nucleate boiling are discussed. An ultrathin vapor chamber based on a wettability patterned evaporator is introduced as a case for the application of the wettability pattern. Besides, modifying the surface with nanostructure to form a multiscale micro/nanostructured surface or superhydrophobic surface also enhances the phase change. Several types of heat spreaders are proposed to investigate the effects of multiscale micro/nanostructured surface and nanostructured superhydrophobic condenser on the thermal performance of the heat spreaders, respectively. The effects of multiscale micro/nanostructured evaporator surfaces with wettability patterns will be analyzed and experimental data will be presented.

Keywords: heat spreader, ultrathin vapor chamber, droplet evaporation, thin-film evaporation, multiscale wick, micro/nanostructure, wettability, wettability pattern, enhance heat transfer

1. Introduction

Two-phase heat spreaders, such as heat pipes, thermal ground planes, and vapor chambers, have been widely used in various areas owing to their high heat transfer efficiency. Improving the thermal performance of the heat spreaders becomes critical for the increasing demand for cooling requirements. Here, we introduce several surface modification techniques for enhancing the heat/mass transfer on heated surfaces and its application on the heat spreaders.

As shown in **Figure 1**, a type of two-phase spreaders, vapor chamber, is composed of wick structure, casing materials, working fluid and vapor core for vapor flow spreading. The evaporator is defined as the casing material and wick structure close to the heat source, while the condenser is defined as the casing material and wick structure close to the heat sink. The heated liquid working fluid in the evaporator vaporizes, spreading to the whole space of the vapor core. The vapor of the working fluid releases heat on the condenser side and condenses into liquid. Then it returns to the evaporator by capillary pressure through wick structure,

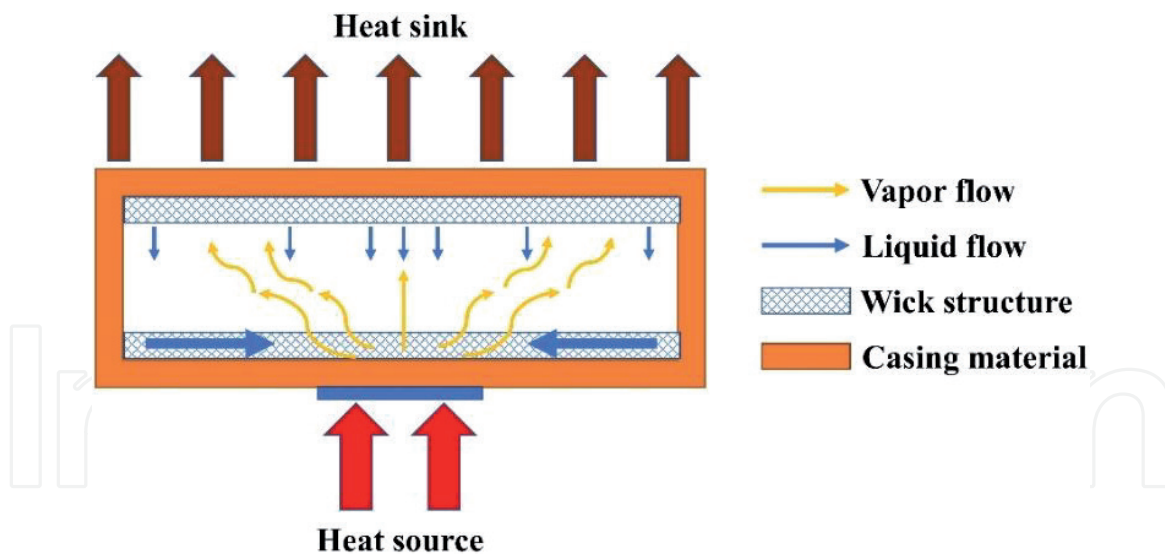


Figure 1.
Schematic of a vapor chamber structure and its working mechanism.

compensating the liquid working fluid of the evaporator. The heat pipe works similarly with the vapor chamber, but it only transfers heat in a one-dimensional way, while the vapor chamber transfers heat both in the horizontal and vertical directions.

Recently, lots of research has been conducted on the fabrication and thermal performance enhancement of the two-phase ultrathin heat spreader. Different casing materials, such as titanium [1], polymer [2, 3], and aluminum [4, 5], were used to develop the thin and light thermal ground plane. However, copper is still the most popular type of casing material for heat spreaders owing to its low cost, high thermal conductivity, and stable chemical characteristics. Thus, most investigations of different wick structures were conducted on the copper-based two-phase heat spreaders. Several types of wick structures were proposed to enhance the thermal performance of thin and ultrathin two-phase heat spreaders, including single arch-shaped sintered-grooved wick [6], bilateral arch-shaped sintered wick [7], mesh-grooved wick [6], pillar-mesh composite wick [8, 9], spiral woven mesh [10], copper fiber [11] and so on.

While many researchers focused on developing a new wick structure or modify wick structure in microscale to enhance the thermal performance of the two-phase ultrathin heat spreader, we tried to use some surface modification methods on the existing evaporator and the wick structure of the evaporator to change its wettability and structure in nanoscale for enhancing the thermal performance. The outline of the chapter is as follows. First, the mechanism of the wettability patterned surface on the nucleate boiling and the droplet evaporation are introduced, respectively. Then, an ultrathin vapor chamber with a wettability patterned evaporator is illustrated as an application case for the wettability patterned surface. After that, the fabrication of a micro/nanostructured surface is introduced and its effect on the wick structure and condenser surface is discussed. The experimental data of several types of heat spreaders with micro/nanostructured surfaces are analyzed.

2. The evaporation enhancement of a multicomponent droplet introduced by chemically wettability patterned surfaces

A molecular dynamic (MD) simulation study proved that the nanoscale wettability patterned surface can enhance the evaporation rate of water [12]. Here, the

authors presented an experimental study to prove the enhancement of the evaporation of a multicomponent droplet also can be provided by a microscale wettability patterned surface.

2.1 Fabrication of the chemically wettability patterned surface

Chemically wettability patterned surface is composed of areas with different wettability. The authors used the method described below to fabricate the chemically wettability patterned surfaces.

A 2 cm × 2 cm prism transparent glass coated with a 100 nm thick Indium tin oxide (ITO) layer is selected as the substrate. ITO layer functions as a resistive heater and its two edges are deposited with 100 nm thick gold electrodes, which are used for wire bonding with a printed circuit board. After the deposition of gold electrodes, the sample is deposited with a 500 nm thick silicon dioxide as a passivation layer. Then a layer of Teflon, which is commonly used as a hydrophobic layer, is spun coated on the top of the silicon dioxide layer, and stabilized following the procedures suggested by DuPont™:

1. A layer of fluorosilane (1H, 1H, 2H, 2H-Perfluorodecyltriethoxysilane, Sigma-Aldrich Co. LLC.) is coated on the silicon dioxide layer to enhance the adhesion between Teflon and silicon dioxide layer. The sample is immersed in a 0.5% volume fraction of fluorosilane solution which used n-hexane as the solvent at least for 1 h. Then the sample is dried and stabilized in a 120°C oven for 1 h to finish the fluorosilane coating;
2. Then, the Teflon (DuPont AF 2401) is coated on the sample by spin-coating at a 1,000 rpm for 1 min;
3. After the spin coating process, the sample is dry in an oven with 40°C for 10 min to remove most of the solvent, 175°C for 10 min to remove 99% of the solvent remains, 250°C (above 5°C glass transition temperature) for 5 min to remove the last trace of the solvent and 330°C for 10 min to reach the maximum uniformity of coating thickness and to enhance the adhesion.

The Teflon layer was patterned to form a chemical wettability patterned surface with the following procedures as shown in **Figure 2**:

1. As the positive photoresist cannot attach to the Teflon, a 30 nm thick alumina layer is formed on the Teflon layer before photoresist coating by 300 cycles of Atomic Layer Deposition at 180°C using the Oxford OpAL ALD in Nanosystem Fabrication Facilities (NFF) in HKUST;
2. HPR506 positive photoresist is coated on the sample by spin coating with a 4,000 rpm for 30 s. Then the sample with a designed photomask is exposed to ultraviolet light with a 240 mJ/cm² energy after the sample is softbaked on a hot plate at 110°C for 1 min. The exposed sample is developed with FHD-5 for 1 min to reveal the pattern and hardbaked in a 120°C oven for 30 min to enhance the durability under dry and wet etching;
3. The unwanted alumina is removed by BCl₃/Cl₂ plasma in the Oxford Plasma Lab 80 Plus Reactive Ion Etcher. Then the unwanted Teflon is removed by O₂ plasma in the same machine;

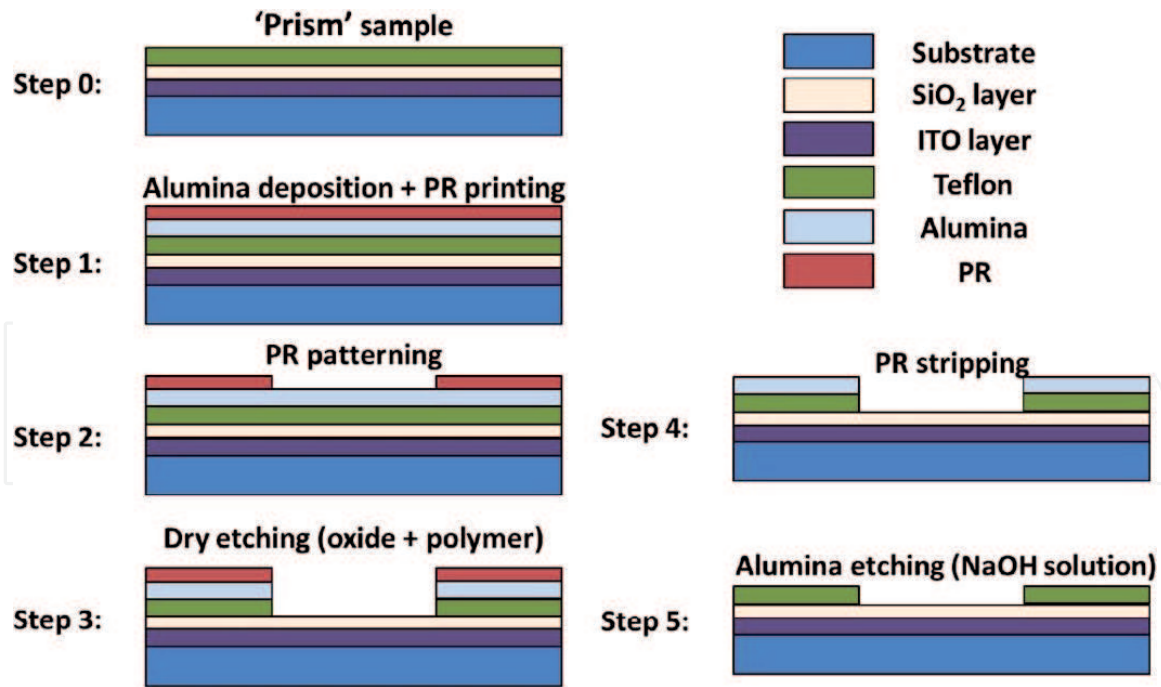


Figure 2. Schematic fabrication procedures of a heterogeneous wetting surface [13].

4. Remain photoresist is removed by MS-2001 (Fujifilm Electronic Materials Co., Ltd.) for 2 min. The processed sample is checked with a microscope using fluorescence light to ensure no photoresist left;

5. Residual alumina is etched away by 5 mol/L NaOH solution for 10 min and the sample is checked with a wettability test.

After all the fabrication procedures are finished, the wettability patterned surface and a typical recording image during the droplet evaporation on the surface are shown in **Figure 3**. The wettability patterned surface is a hydrophilic surface (silicon dioxide on the prism glass) with square Teflon hydrophobic islands of $D = 50 \mu\text{m}$ and pitch distance of $L = 100 \mu\text{m}$.

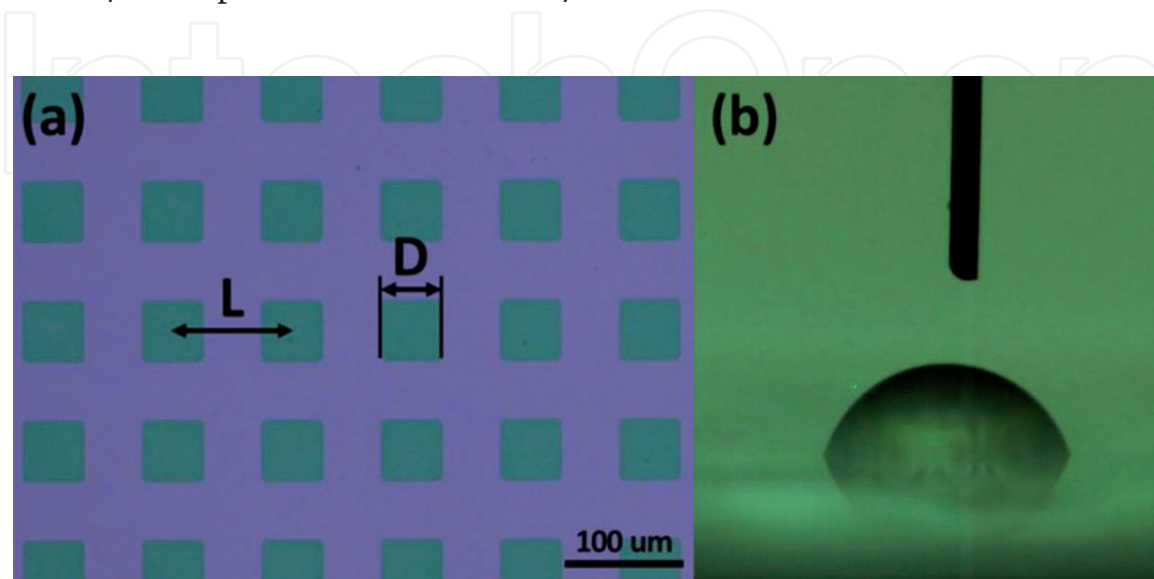


Figure 3. (a) Microscopic image of a wettability patterned surface and (b) a typical recording image during the droplet evaporation on the surface [14].

The roughness of the sample is measured by a surface profiler (Dektak 150 Veeco). The roughness of the Teflon and the substrate is only 5 nm and 25 nm, respectively. Thus, its effect on evaporation is negligible. Finally, the sample is bonded on a Printed circuit board (PCB) for the experiments of multicomponent droplet evaporation with different sample temperatures.

2.2 Experimental setup and procedure of the droplet evaporation

The experimental setup is presented in **Figure 4(a)**. A Charge-coupled device (CCD) camera (MotionXtra HG-100 K, Redlake Co., Ltd.) with a long-distance zoom lens (Zoom 6000, Navitar Inc.) is adopted for recording the evaporation process to investigate the droplet evaporation characteristics including dynamic contact angle, base diameter, and evaporation duration of a droplet. Because the droplet profile is high symmetric, the focus plane of the camera is suitable to adjust to the cross-section of the droplet, as shown in **Figure 4(b)**. The droplet profile image is analyzed by a snake-based approach, which is shown in **Figure 4(c)**. Besides, the microscopic motion of the contact line is recorded by an inverted microscope (Eclipse TE2000-U, Nikon Instruments Inc.) connected to the CCD camera.

The droplet for the testing is generated by mixing deionized water and ethanol with an ethanol concentration varied from 0 vol. % to 15 vol. %. The droplets for each experiment are freshly generated before the test and the accuracy of the ethanol concentration is ± 0.05 vol. %. The sample is heated and controlled at 40°C by a direct current (DC) power supply with a proportional-integral-derivative (PID) controller. The temperature difference between Teflon and the silicon dioxide layer

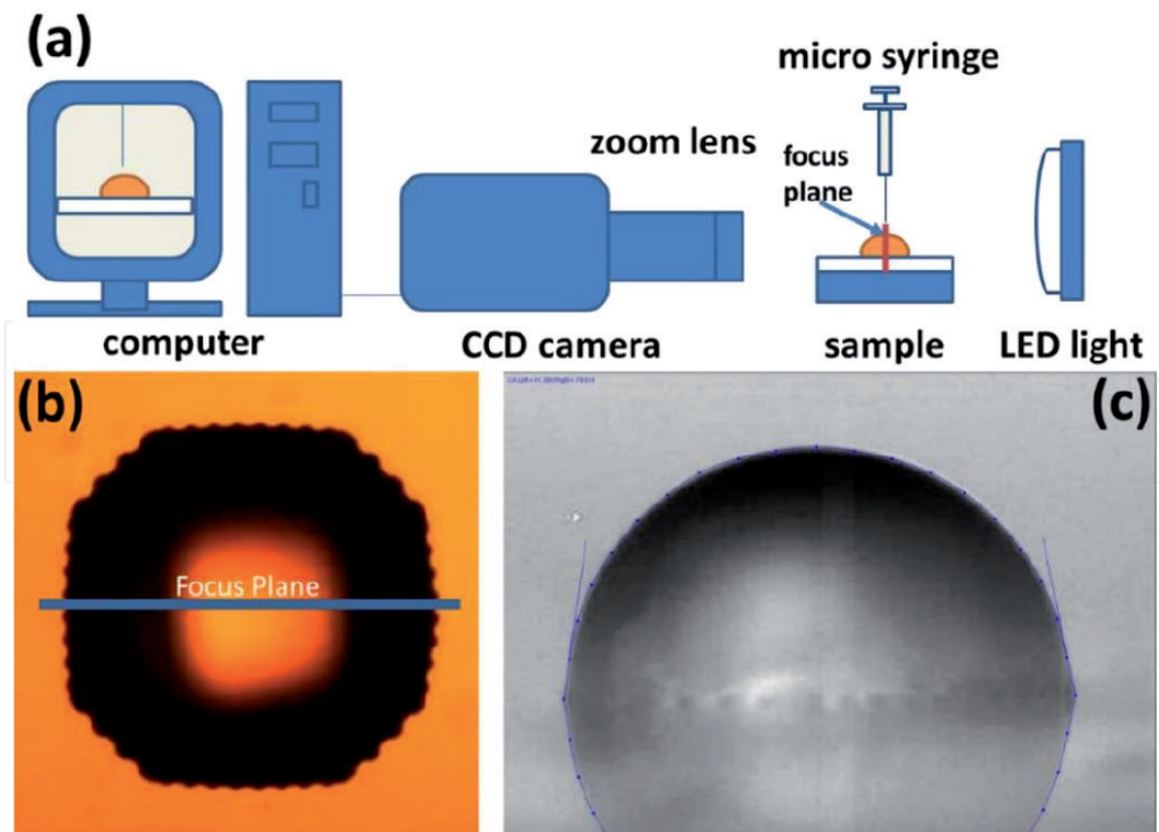


Figure 4. Experimental setup and contact angle measurement for the droplet evaporation: (a) schematic of the experimental setup for the droplet evaporation; (b) bottom view of the droplet on a wettability patterned surface and corresponding focus plane of the contact angle measurement; and (c) the contact angle measurement result by the snake-based approach [14].

is negligible as the thickness of Teflon is only around 60 nm. Only if the sample is kept at 40°C for 5 min the test can be started.

The $1 \mu\text{l} \pm 0.05 \mu\text{l}$ multicomponent droplet is produced by a Hamilton micro-syringe (Hamilton, 5 μl TLC syringe with a removable needle of gauge 33, 210 μm of outside diameter) and gently put on the heated homogenous or heterogeneous wettability surfaces. The location of the droplet is the same in every test to ensure the reproducibility of the experiments. After the droplet is put on the sample surface, the CCD camera starts to record the profile of the evaporation droplets or the microscopic motion of the contact line with the inverted microscope until the droplet vaporizes totally. To avoid the trace of the vaporized droplet affecting the next test, the sample is cleaned with acetone, ethanol, and deionized water, and dried with compressed air flow followed by a 105°C bake for 10 min in an oven. To ensure reproducibility, the location of the droplet is the same in every test and the whole experimental setup is kept at $23 \pm 1^\circ\text{C}$ and $50 \pm 3\%$ RH environment without any airflow. Besides, more than five times each experiment is conducted to identify reproducibility.

A hydrophilic surface, which is form by depositing only a layer of silicon dioxide on the sample, is chosen as a reference to investigate the enhancement effect because a homogenous hydrophilic surface always had a higher evaporation rate than that of a homogenous hydrophobic one [15].

2.3 Experimental result and discussion on the evaporation enhancement induced by a wettability patterned surface

First, the wettability of the multicomponent droplets on a hydrophilic (SiO₂), hydrophobic (Teflon), and wettability patterned surfaces at 40°C are measured to confirm the wettability, as shown in **Table 1**.

Then, the evaporation duration of the droplets is recorded and shown in **Figure 5**. The evaporation duration of a droplet on a wettability patterned surface is around 10% shorter than that on a hydrophilic surface. Changing the ethanol concentration has an insignificant effect on the evaporation duration. The increase of the ethanol concentration leads to a shorter evaporation duration, which is contributed from the latent heat of ethanol is only 1/3 of water. In summary, the wettability patterned surface enhances the evaporation rate when compared with a hydrophilic surface.

The increase of the contact line length introduced by the wettability patterned surface plays a critical role in the enhancement. First, the mass flux of the evaporating flux ($j(x)$) of a slowly evaporating droplet on a hydrophilic surface can be calculated by [16]:

$$j(x) = j_0 \left[1 - \left(\frac{x}{r_s} \right)^2 \right]^{\frac{1+\theta/\pi}{2}} \quad (1)$$

Where, θ ($0 < \theta < \pi/2$) is the instant contact angle during the evaporation, x is the length from the center of the drop which has a radius r_s . The factor of mass flux vapor (j_0) depends on the saturation pressure, vapor diffusivity, and far-field concentration. According to Eq. (1), the distribution of the evaporation flux for a droplet on a hydrophilic surface is non-uniform. The highest evaporation flux occurs at the contact line and it was also confirmed by Hu and Larson [17]. Besides, they derived an expression of the total evaporation rate of a droplet on a hydrophilic surface, which is:

$$m(t) = -\pi R D (1-H) c_v (0.27\theta^2 + 1.30) \quad (2)$$

Ethanol concentration (vol.%)	Hydrophilic surface			Hydrophobic surface		Patterned surface
	Receding contact angle (°)	Advancing contact angle (°)	Initial contact angle (°)	Receding contact angle (°)	Advancing contact angle (°)	Initial contact angle (°)
0	62.1	88.7	78.6	84.5	134.9	82.1
5	54.8	82.5	75.0	78.3	130.5	78.5
10	45.7	75.8	69.3	67.5	127.2	73.4
15	33.2	71.2	59.5	61.1	124.1	69.0

Table 1. Wettability data of the wettability patterned surface and the reference homogenous wettability surfaces under 40°C sample temperature [14].

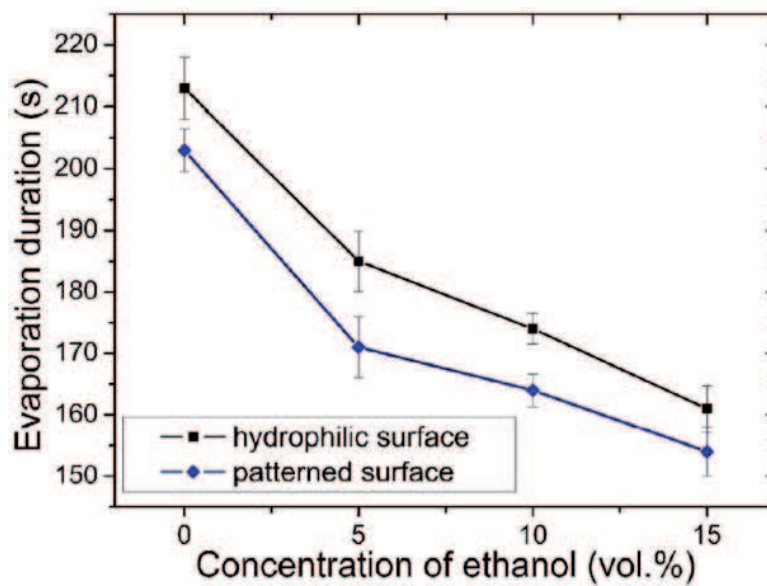


Figure 5. Evaporation duration of a droplet with a range of ethanol concentration from 0 vol.% to 15 vol.% on homogenous (hydrophilic) and heterogeneous (wettability patterned) surfaces [14].

Where, R is the contact-line radius, D is the vapor diffusivity, and $(1-H)c_v$ is the vapor concentration difference. From Eq. (2) we can know the total evaporation rate is proportional to the perimeter of the contact line. Thus, the evaporation rate will be enhanced if the contact line is elongated. The wettability patterned surface increases the length of the contact line according to our observation, as shown in **Figure 6**. The spreading of the contact line is obstructed by the hydrophobic islands, leading to an elongation of the contact line along the islands' edge. Thus, although the contact area of a droplet on the wettability patterned surface is decreased, the length of the contact line is prolonged, resulting in faster evaporation of the droplet when compared with a homogenous hydrophilic surface under the same conditions. Moreover, a molecular dynamics simulation study also showed the increase of the total length of the hydrophobic island boundary in a nanoscale hydrophobic-hydrophilic pattern surface leads to an enhancement of the total evaporation rate [12].

Evaporation has been confirmed as the main phase-change mode in the evaporator of a two-phase heat spreader when the heat flux is less than 100 W/cm². Especially, thin-film evaporation which occurs nears the contact line contributes at

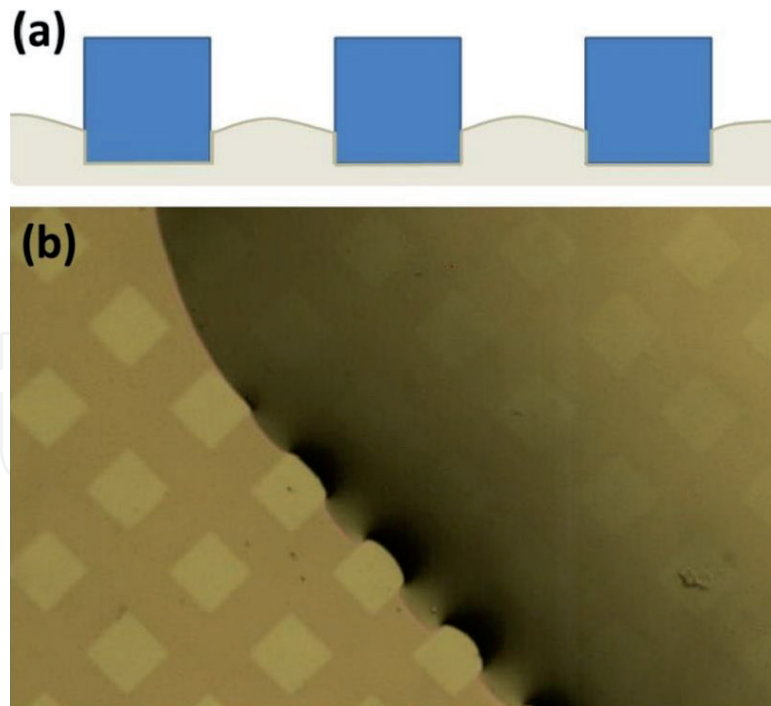


Figure 6. The contact line profile of a multicomponent droplet (15 vol.% ethanol) on the wettability patterned surface: (a) the schematic of the contact line and (b) microscopy image [14].

least 50% even more than 80% of the total heat transfer in the evaporator [18–21]. Therefore, if the wettability patterned surface can be integrated into the evaporator of a two-phase heat spreader, the evaporation rate may be enhanced owing to the increase of thin-film evaporation are introduced by the elongated contact line. Then the thermal performance of the two-phase heat spreader can be enhanced. In the following section, an ultrathin vapor chamber with a wettability patterned surface integrated into the evaporator is presented. The effect of the wettability pattern on the thermal performance of the ultrathin vapor chamber will be discussed.

3. An asymmetric ultrathin vapor chamber with a wettability patterned surface on its evaporator

As shown in **Figure 7**, three types of ultrathin vapor chambers are designed and fabricated to investigate the effect of wettability pattern surface on the thermal performance of the ultrathin vapor chambers. The fabrication and the evaluation methods for the ultrathin vapor chamber are introduced. Multiscale micro/nano-structured wick structure is also adopted in the ultrathin vapor chamber and its effect will be also discussed in the next section.

3.1 Design and fabrication of the ultrathin vapor chambers with wettability patterned surface on its evaporator

Figure 7(a) presents the cross-section schematic of the ultrathin vapor chamber for case 1. Ultrathin copper (C1100P, 99.9%) is selected as the casing material and the #500 stainless-steel (SS 304) mesh covered with a layer of copper is adopted as the wick structure. A square array of micropillars integrated into the inner surface of the condenser is used for supporting the space of the vapor core. To investigate the effect of a multiscale micro/nanostructured surface, the only difference

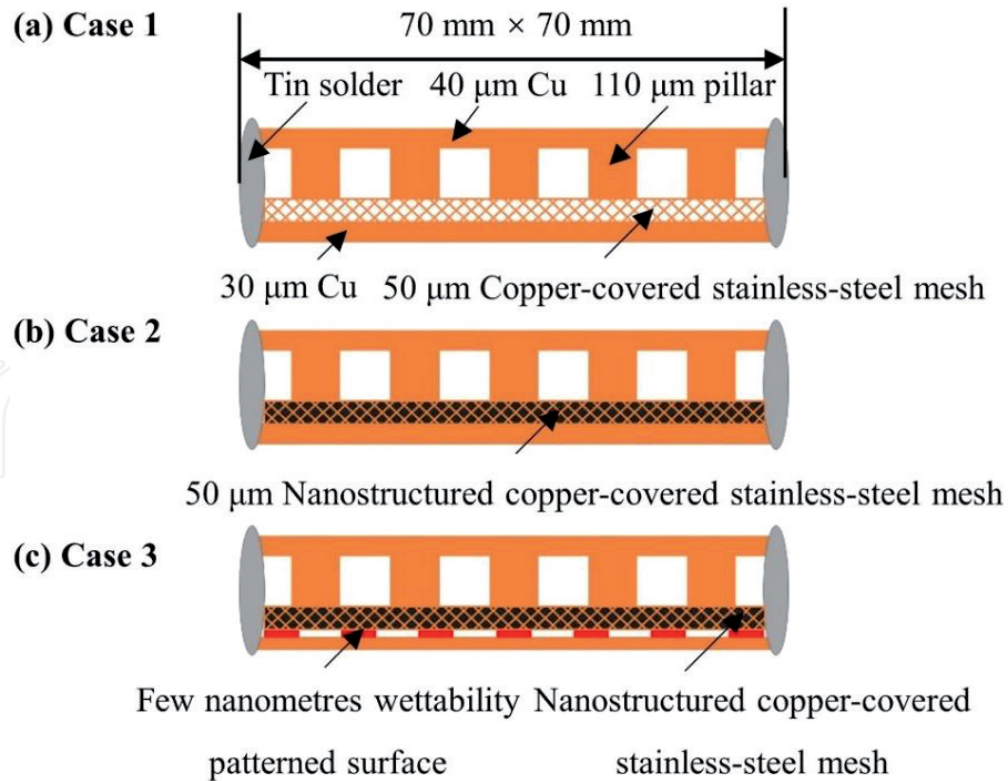


Figure 7.
 The cross-section prototypes schematic of three ultrathin vapor chambers [22].

between case 1 and case 2 is the wick structure of case 2 is nanostructured to form a multiscale micro/nanostructured surface, as shown in **Figure 7(b)**. Case 3 which is shown in **Figure 7(c)** is developed based on the structure of case 2. A wettability pattern is fabricated on the inner surface of the evaporator casing material to examine its effect.

The square array of micropillars is fabricated through photolithography and electroplating, which is described below and shown in **Figure 8(a)**:

1. A 40 μm copper foil is cleaned with acetone, isopropanol, and DI water ultrasonic in sequence to remove organic contaminants. Then it is immersed into 20% sulfuric acid to dissolve the native oxide layer on its surface;

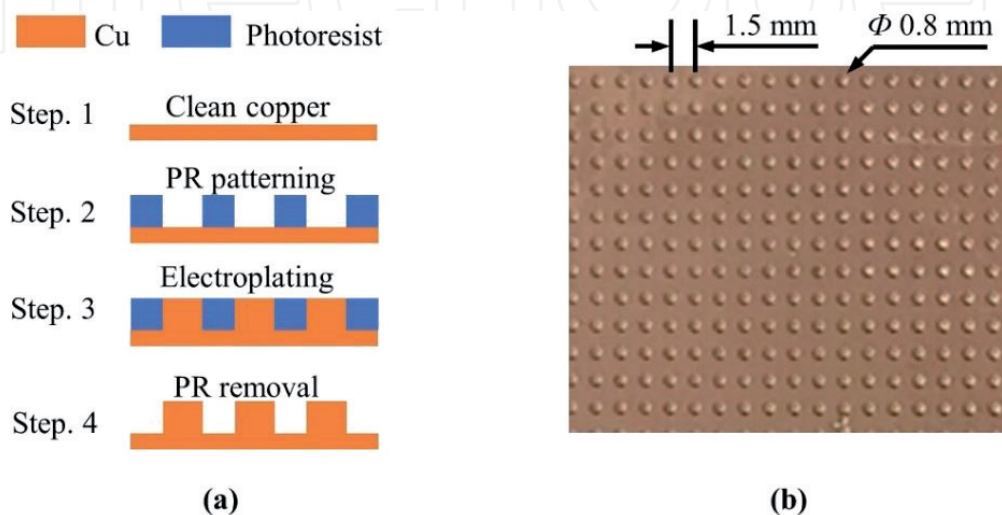


Figure 8.
 (a) the fabrication procedures of the micropillar array and (b) the picture of micropillar array [22].

2. A positive photoresist AZ9260 is coated on the cleaned copper by spin-coating at 2,000 rpm for 30 s. Then the coated copper is softbaked on a 110°C hot plate for 3 min to remove most solvent in the photoresist. To ensure the exposure quality of the photoresist pattern mask, the copper should be put in an environment with a more than 60% RH for 10 min to do the rehydration process before the exposure. After that, the coated copper with a chromium photo-mask is exposed with 1200 mJ/cm² energy and then developed in an AZ400K developer diluted with 4 parts of water for 2 min. A microscope with fluorescent light is used to check the development quality. In the final of this step, a 120°C hardbaked for 30 min is adopted to enhance the adhesion between photoresist and copper for a long time electroplating process;
3. The photoresist patterned copper is immersed in an electroplating tank to do the electroplating process. The current is set at 0.07 A and the electroplating duration is around 15 h. When the electroplating process is completed, the micropillar shows a height of 110 μm and a diameter of 0.8 mm, as shown in **Figure 8(b)**. The pitch distance between two nearby micropillars is 1.5 mm;
4. The copper is immersed in MS2001 at 70°C for 5 min in Nanosystem Fabrication Facility-Hong Kong University of Science and Technology to remove the photoresist and the fabrication process is finished.

The wick structure of case 1, copper-covered #500 stainless-steel (SS 304) mesh (wire diameter: 25 μm, wire spacing: 25 μm) is fabricated with the following method. First, the mesh is activated at a current of 2 A for 2 min in a stainless-steel electroplating activation solution (From Beichen Limited Company, China) to enhance the bonding quality between the electroplated copper layer and the stainless-steel mesh. Then, the copper layer is formed by electroplating in a stationary solution with 0.8 M CuSO₄ and 1.5 M H₂SO₄ at a current of 1 A for 5 min, as shown in **Figure 9(a)**. The nanostructured copper-covered stainless-steel mesh of case 2 is fabricated by oxidizing the copper layer through a chemical surface modification method [23]. The method is firstly immersing the copper-covered stainless-steel mesh into an aqueous solution with 0.065 M K₂SO₈ and 2.5 M KOH at 70°C for 30 min. Then the mesh is rinsed with water and dried in a 180°C oven for 1 h. A flower-like nanostructure is grown on the surface of the copper layer, as shown in **Figure 9(b)**.

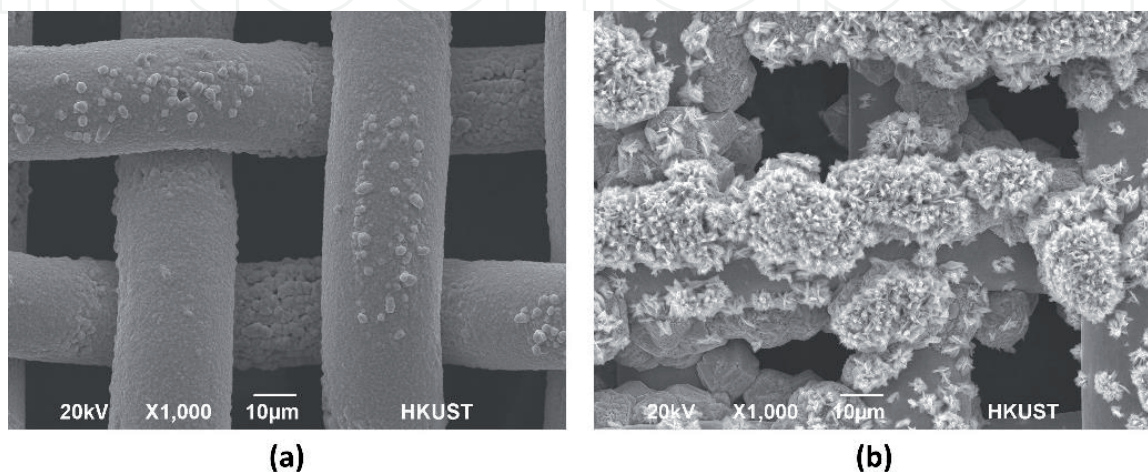


Figure 9.
 (a) The stainless-steel mesh with a layer of copper and (b) the mesh with a layer of flower-like nanostructure [22].

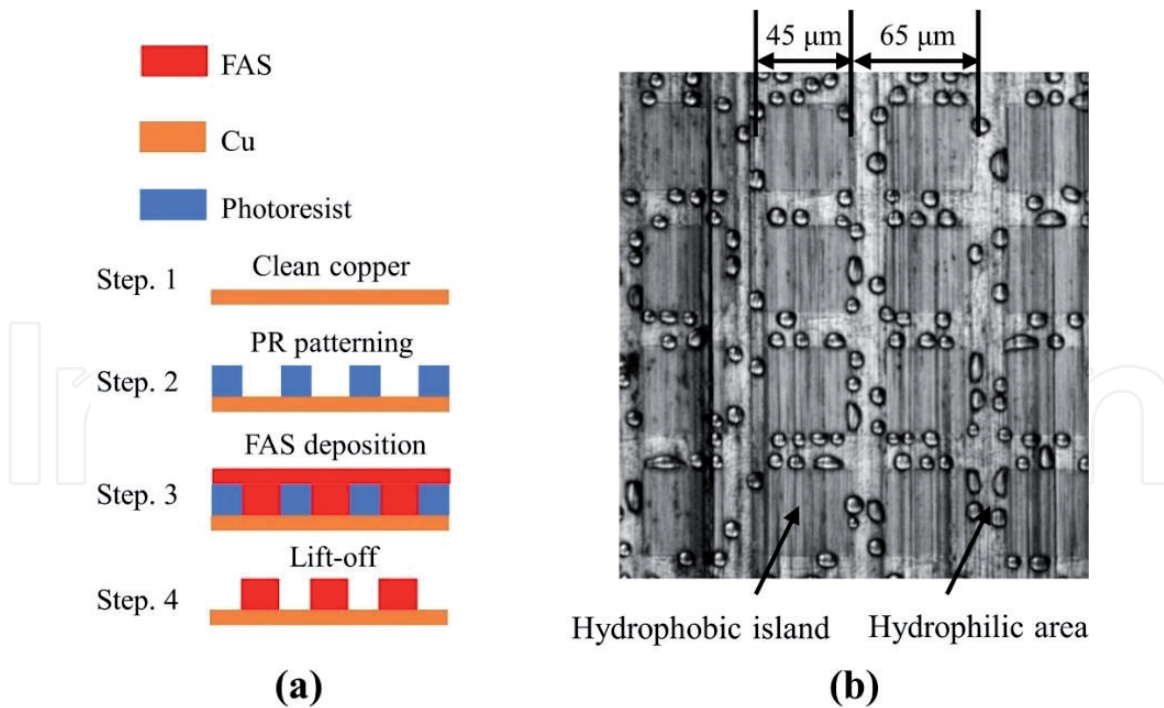


Figure 10.
 (a) The fabrication procedures of a wettability pattern and (b) wettability check of a wettability patterned surface [22].

The wettability patterned surface for case 3 is fabricated with the following method, as shown in **Figure 10(a)**:

1. A 30 μm copper foil is firstly cleaned with the method described in the fabrication of the micropillar array;
2. A positive photoresist HPR506 is coated on the copper by spin-coating at 4,000 rpm for 30 s. Then the photoresist-coated copper is softbaked on a 110°C hot plate for 1 min. After that, the copper with a chromium photomask is exposed with 120 mJ/cm^2 energy and then developed in an FHD-5 develop for 1 min to reveal the photoresist pattern;
3. The photoresist patterned copper is immersed into a 1H, 1H, 2H, 2H-Perfluorodecyltriethoxysilane (FAS-17) solution and baked in a 120°C oven to form a hydrophobic layer which shows a 110° water contact angle and only a monolayer thickness [24]. The solvent of the Fluorosilane (FAS) solution is n-hexane, and the mass ratio of FAS is 1.6%;
4. The FAS-treated copper is immersed into an acetone solution to do the lift-off process. The parts with photoresist are dissolved into acetone. Thus, the FAS layer on the top of the photoresist is also removed. Then a wettability pattern is fabricated on the surface of copper.

Figure 10(b) shows a wettability check method using the condensation of water. The vapor condenses on the hydrophilic area, proving the success of the fabrication. The wettability pattern is composed of hydrophobic islands with a 45 μm side length and a 65 μm pitch distance between two nearby islands.

After the fabrication of all components, the mesh is sandwiched between the bottom and top casings, and then it is sealed by SnAg (97/3) solder. A tiny copper tube is connected to the inside of the chamber for the evacuating and feeding process. The dimensions of ultrathin vapor chambers are summarized in **Table 2**.

Item	Dimension
Bottom copper casing material (C1100P)	70 mm × 70 mm × 0.03 mm
#500 stainless-steel mesh (SS304)	60 mm × 60 mm × 0.05 mm
Micropillar array	70 m × 70 m × 0.1 mm
Micropillar diameter	0.8 mm
Pitch distance of the micropillars	1.5 mm
Top copper casing material (C1100P)	70 mm × 70 mm × 0.04 mm
Hydrophobic island side length (d)	45 μm
Pitch distance of the hydrophobic islands (P)	65 μm
The Thickness of the wettability pattern	1.34 nm

Table 2.
Dimensions of ultrathin vapor chambers [22].

3.2 Experimental setup of the thermal performance test for the ultrathin vapor chamber

When the assembly of the ultrathin vapor chamber is completed, a certain amount of water is filled into the inner space of the vapor chamber before the experimental tests. The vapor chamber is evacuated to 1 Pa and filled with different charge ratio η , which is defined as:

$$\eta = \frac{V_{water}}{V_{total}} \times 100\% \quad (3)$$

Where, V_{water} is the volume of water inside the vapor chamber and V_{total} is the total volume of the inner space for the vapor chamber. As shown in **Figure 11(a)**, the evacuated ultrathin vapor chamber only has a less than 200 μm thickness.

The LW-9510 vapor chamber thermal performance measurement apparatus (LongWin Co., Ltd.) is adopted for evaluating the thermal performance of the vapor chamber. The vapor chamber is heated at the evaporator side by a heater with an 8 mm × 8 mm footprint and cooled on the outer surface of the condenser by an adjustable cooling fan with a 6.875 cfm flow rate at 22°C room temperature, as shown in **Figure 11(b)**. Besides, Teflon material is used as thermal insulation materials to reduce heat loss, making the maximum heat loss is only 0.41 W in the tests. One T-type thermocouple is attached to the center of the condenser outer surface (T_1) and 4 T-type thermocouples are attached at the side of the surface (T_2 , T_3 , T_4 , and T_5), as shown in **Figure 11(c)**. A T-type thermocouple Five is inserted into the block below the center of the evaporator with a 1 mm distance to measure the heater temperature (T_h), which is shown in **Figure 11(d)**.

The authors examine the thermal performance of the ultrathin vapor chambers in the horizontal and vertical direction using horizontal thermal resistance (R_{hr}) and vertical thermal resistance (R_{vr}), respectively, which are defined as:

$$R_{hr} = \frac{T_1 - T_{avg(2-5)}}{Q} \quad (4)$$

$$R_{vr} = \frac{T_b - T_{avg(1-5)}}{Q} \quad (5)$$

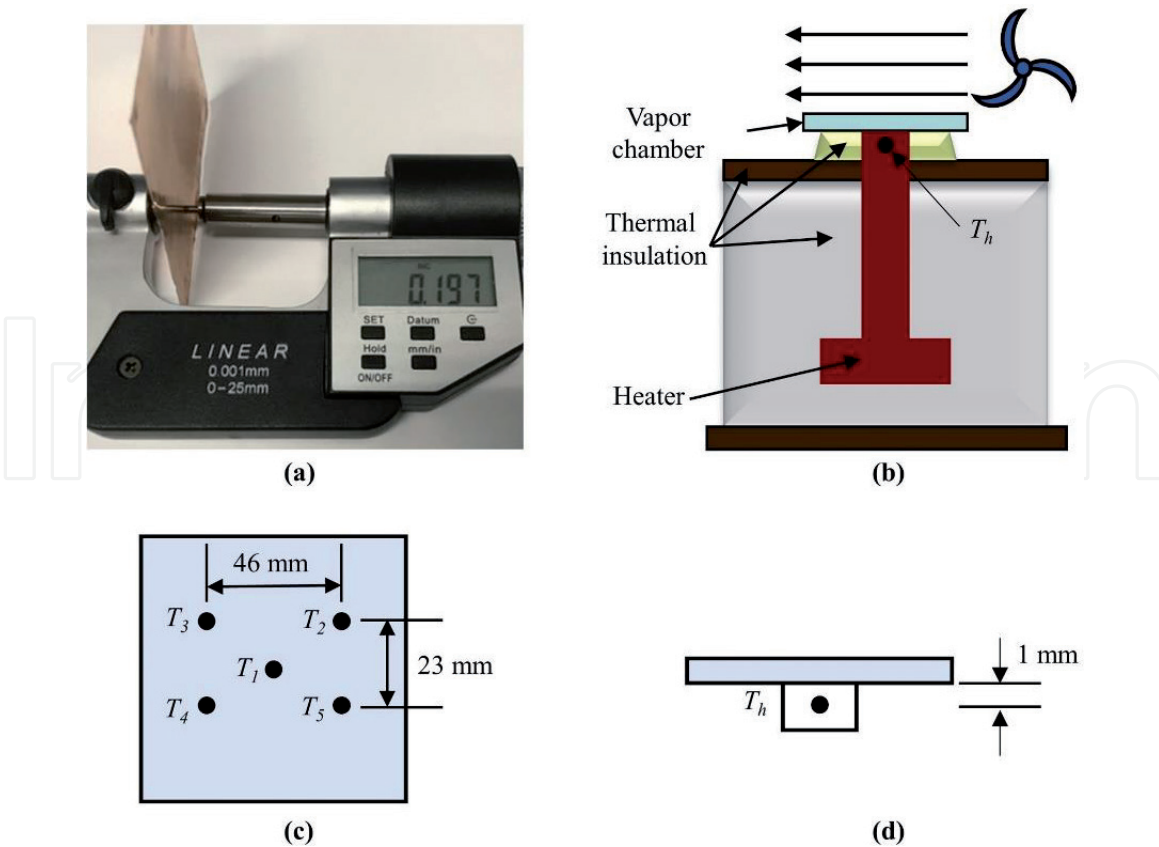


Figure 11. (a) The thickness of an evacuated ultrathin vapor chamber and the schematic of the experimental setup; (b) apparatus; (c) temperature measurement points on the top of the vapor chamber; and (d) heater temperature measurement [22].

Where, Q is the input power measured by a power sensor of the LW9510, $T_{\text{avg}(1-5)} = (T_1 + T_2 + T_3 + T_4 + T_5)/5$ and $T_{\text{avg}(2-5)} = (T_2 + T_3 + T_4 + T_5)/4$. T_b is the temperature at the center of the evaporator outside surface, which is calculated based on Fourier's law:

$$T_b = T_h - ql / k_{\text{Cu}} \quad (6)$$

where l is the distance from the location of T_h to the center of the evaporator outside surface, which has a value of 0.001 m. k_{Cu} is the thermal conductivity of copper with a value of 401 W/(m·K). q is the input heat flux, which is defined as:

$$q = Q / A_h \quad (7)$$

Where, A_h is the footprint of the heater.

For characterizing the temperature uniformity of the vapor chamber and comparing it with copper, other materials, or commercial vapor chambers, the in-plane effective thermal conductivity (K_{eff}) is defined as:

$$K_{\text{eff}} = k_{\text{Cu}} R_{\text{hr,Cu}} / R_{\text{hr,vc}} \quad (8)$$

Where, $R_{\text{hr,Cu}}$ is the measured horizontal thermal resistance of copper.

The uncertainties are calculated based on the indirect parameter uncertainty analysis: if $F = F(x_1, x_2, \dots, x_n)$, the uncertainty of F can be calculated by:

$$U_F = \left[\left(\frac{\partial F}{\partial x_1} U_1 \right)^2 + \left(\frac{\partial F}{\partial x_2} U_2 \right)^2 + \dots + \left(\frac{\partial F}{\partial x_n} U_n \right)^2 \right]^{1/2} \quad (9)$$

Where U_1, U_2, \dots, U_n are the uncertainties of x_1, x_2, \dots, x_n , respectively. The maximum uncertainty of the heat flux q , horizontal thermal resistance R_{hr} and vertical thermal resistance R_{vr} under 95% confidence level are $\pm 0.4\%$, $\pm 6.1\%$, and $\pm 2.5\%$, respectively.

3.3 Effect of the wettability patterned surface on the thermal performance of the ultrathin vapor chamber

Figure 12 presents the experimental results of the thermal performance of the ultrathin vapor chambers. In this section, the thermal performance of the vapor chamber case 2 and case 3 are compared with each other to investigate the effect of wettability patterned surface as the only difference between them is whether a wettability pattern is integrated into the evaporator or not.

Figure 12(c) and **(e)** show the horizontal thermal resistance of the vapor chamber case 2 and case 3, respectively. The horizontal thermal resistance of case 2 for all the charge ratios first quickly decreases with the increase of the heat flux from 8.59 W/cm^2 to 14.53 W/cm^2 . Then it gradually decreases when the heat flux increases from 14.53 W/cm^2 to 23.91 W/cm^2 . On the other hand, the horizontal thermal resistance always decreases with the decrease of the charge ratio at a certain heat flux. Thus, the minimum horizontal thermal resistance exists at the 23.91 W/cm^2 heat flux of 60.4% charge ratio, which is 0.170°C/W . Compared with case 2, case 3 shows a similar trend but a lower horizontal thermal resistance under the same test conditions. For example, the horizontal thermal resistance at the 8.59 W/cm^2 of 60.4% charge ratio is 0.666°C/W for case 2 while it is only 0.295°C/W for case 3, which is only 44.3% of the previous. The minimum horizontal thermal resistance of case 2 is only 0.055°C/W occurring at 23.91 W/cm^2 heat flux of 60.4% charge ratio. The comparison proves integrating a wettability pattern to the inner surface of the evaporator of the ultrathin vapor chamber can greatly enhance the horizontal thermal performance of the ultrathin vapor chamber.

Figure 12(d) and **(f)** present the vertical thermal resistance of the vapor chamber case 2 and case 3, respectively. The vertical thermal resistance of case 2 for large charge ratio (65.2, 67.6, and 70.1%) gradually decreases with the increases of the heat flux, proving case 2 with large charge ratios does not reach the partial dry-out condition. When the charge ratio is less than 65.2%, case 2 starts partial dry-out at the heat flux of 23.91 W/cm^2 , due to an insufficient amount of water returning to the evaporator. Though a small charge ratio gives a lower vertical thermal resistance if partial dry-out does not happen, the minimum thermal resistance for large charge ratios is close to that for the small charge ratio. This is because case 2 with a large charge ratio can work at a higher heat flux, leading to a further decrease of the vertical thermal resistance. The minimum vertical thermal resistance of case 2 is 1.37°C/W , happening at the heat flux of 19.84 W/cm^2 of 62.8% charge ratio. However, though the trend of the vertical thermal resistance of case 3 is similar to case 2, case 3 does not show an improvement of the vertical thermal performance. When the charge ratio is small (60.4% and 62.8%), case 3 starts partial dry-out at a lower heat flux which is 19.84 W/cm^2 . Besides, the vertical thermal resistance for all the charge ratios at a certain heat flux of case 3 is larger than that of case 2. The minimum thermal resistance for case 3 is just 1.54°C/W at 23.91 W/cm^2 heat flux of 70.1% charge ratio. Therefore, the evaporator integrated with the wettability

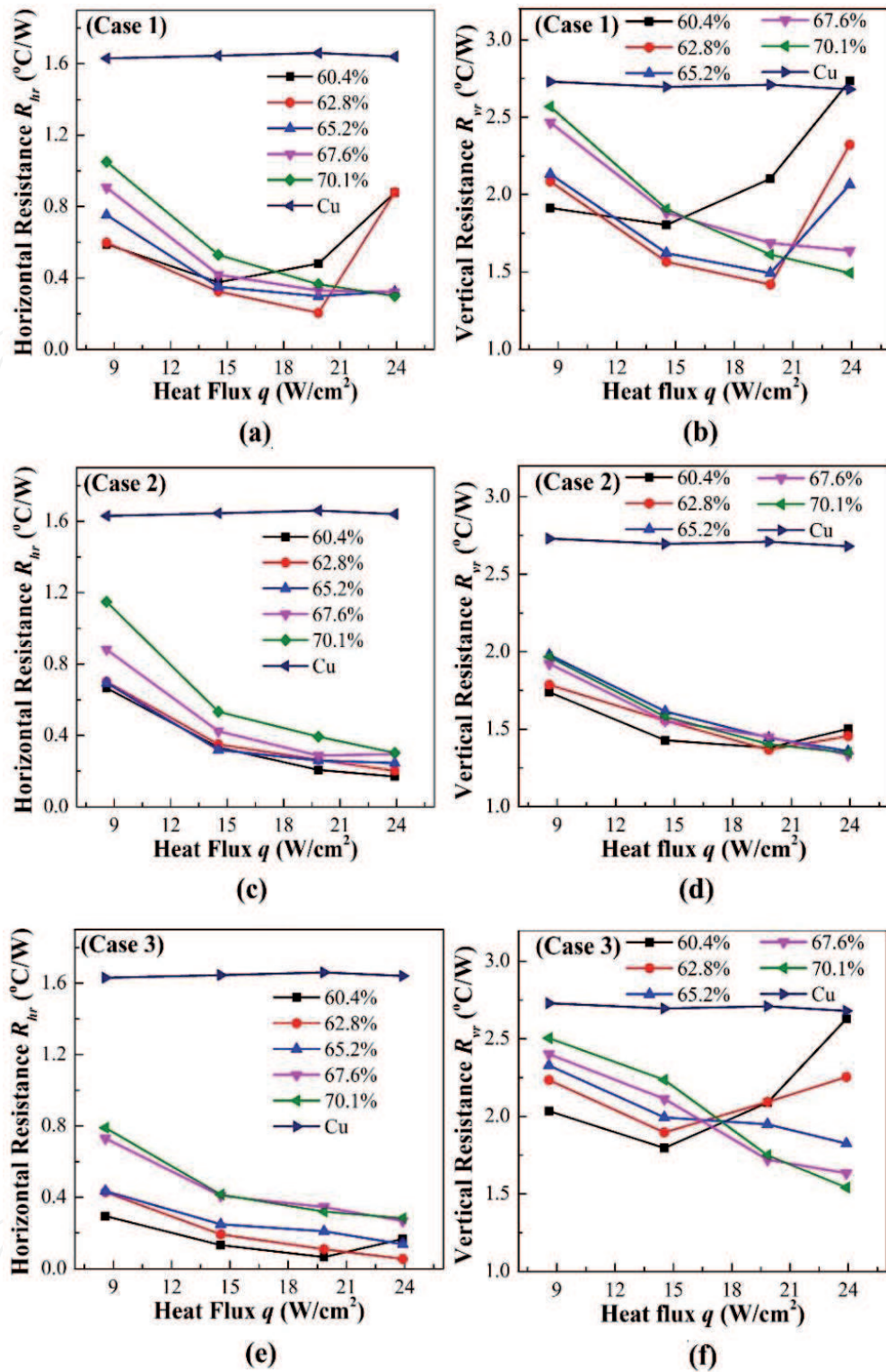


Figure 12. Thermal performance of the ultrathin vapor chambers: Horizontal thermal resistance (a), (c), and (e); vertical thermal resistance (b), (d), and (f) [22].

pattern does not enhance the vertical thermal performance in this study. One possible reason is the large area of hydrophobic islands deteriorates the backflow ability of the wick structure. The capillary pressure determined the backflow ability of the wick structure, which can be calculated by [22]:

$$P_{Cap.} = \frac{2\sigma\cos\theta}{r_{eff}} \quad (10)$$

where σ is the surface tension of the working fluid, r_{eff} is the effective radius of the wick structure and θ is the working fluid contact angle on the wick structure. Since part of the working fluid returns to the evaporator through the interface between the wick structure and the wettability patterned surface, the contact angle may be larger considered the effect of hydrophobic islands. Moreover, the area fraction of hydrophobic islands in this study reaches 47.9%, giving that $\cos\theta$ in Eq. (10) for case 3 may be much smaller than that for case 2. Thus, the backflow ability of the wick structure for case 3 is poorer than that of case 2, leading to lower cooling performance. Another possible reason is the photoresist, which may be left on the surface after the fabrication, releases non-condensable gas during the tests and deteriorate the backflow ability due to its hydrophobicity. Therefore, optimizing the design of the fabrication process may improve the vertical thermal performance of the ultrathin vapor chambers.

Generally, a wettability pattern can greatly enhance the temperature uniformity and is also promising to lower the vertical thermal resistance of a vapor chamber. In the next section, the authors will present that only changing the wettability of the condenser can also improve the temperature uniformity of a vapor chamber.

4. An asymmetric vapor chamber with a nanostructured superhydrophobic condenser

Compared with filmwise condensation occurring at a hydrophilic surface, dropwise condensation induced by a hydrophobic surface can largely increase the condensation heat transfer rate both under vacuum and atmosphere conditions [25]. Therefore, integrating a hydrophobic surface to the condenser of a vapor chamber is promising to enhance the thermal performance of the vapor chamber. In this section, the design and fabrication of a 70 mm \times 70 mm \times 3 mm asymmetric vapor chamber with a nanostructured superhydrophobic condenser are introduced firstly. Then the effect of the nanostructured superhydrophobic surface is discussed based on the experimental results.

4.1 Design, fabrication, and thermal performance test of the vapor chamber

Figure 13(a) illustrates the design of the vapor chamber. To compare the thermal performance with a conventional vapor chamber, the major difference between the proposed one and the conventional one is the wick-laid condenser for the conventional one is replaced by a nanostructured superhydrophobic condenser.

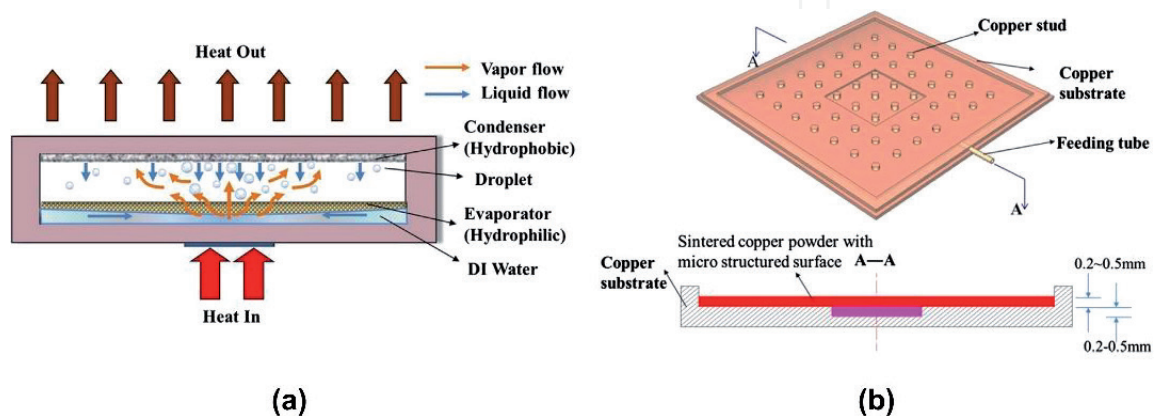


Figure 13. (a) The schematic of the vapor chamber with a nanostructured superhydrophobic condenser and (b) the schematic of the evaporator base [26].

As shown in **Figure 13(b)**, the evaporator base with an area of $70 \times 70 \text{ mm}^2$ is made of oxygen-free copper with a special configuration: (1) An array of studs is uniformly distributed on the copper substrate to prevent distortion caused by the pressure difference between the inner space of the vapor chamber and atmosphere; (2) A rectangular slot is set at the center of the substrate for sintering fine copper powders to enlarge capillary pressure in the center of the evaporator; and (3) A feeding tube is installed at the edge of the substrate to evacuate and feed working fluid. To fabricate the wick structure of the evaporator, a layer of size $57 \mu\text{m}$ copper powder is put into the center rectangular slot and then a layer of size $100 \mu\text{m}$ copper powder is covered the overall substrate. After that, a sintering process of the wick structure is performed in a 975°C hydrogen/nitrogen atmosphere for 2.5 h. This composite wick structure has an excellent backflow ability to prevent the occurrence of the partial dry-out as the smaller pores in the central wick provide higher capillary pressure.

The nanostructure of the condenser surface is fabricated with the method described in Section 3.1. Then, the nanostructured condenser is coated with a monolayer of FAS-17 using the method also described in Section 3.1. **Figure 14** shows the water contact angle of the condenser and the view of the flower-like nanostructure.

The thermal performance evaluation experimental setup is conducted on the LW-9510 platform which is described in Section 3.1. As the test power is much larger than that for the ultrathin vapor chamber, the cooling fan is replaced by a $170 \times 80 \text{ mm}^2$ aluminum block attached to the outside surface of the condenser. The temperature of the aluminum block is set at 35°C and controlled by a water circulation system. Besides, the heater size is changed to $15 \text{ mm} \times 15 \text{ mm}$. In this study, the authors use the same parameter as that for the ultrathin vapor chamber, horizontal and vertical thermal resistance, to assess the thermal performance of this vapor chamber. The uncertainty of the heat load, temperature measurement, and the length measurement is $\pm 0.1\%$, $\pm 0.2\%$, and $\pm 0.4\%$, respectively [26].

4.2 The effect of the nanostructure condenser on the thermal performance of the vapor chamber

The thermal performance of the asymmetric vapor chamber is compared with that of a conventional vapor chamber and a copper with the same dimensions, as shown in **Figure 15**. The charge amount of the asymmetric vapor chamber is set at

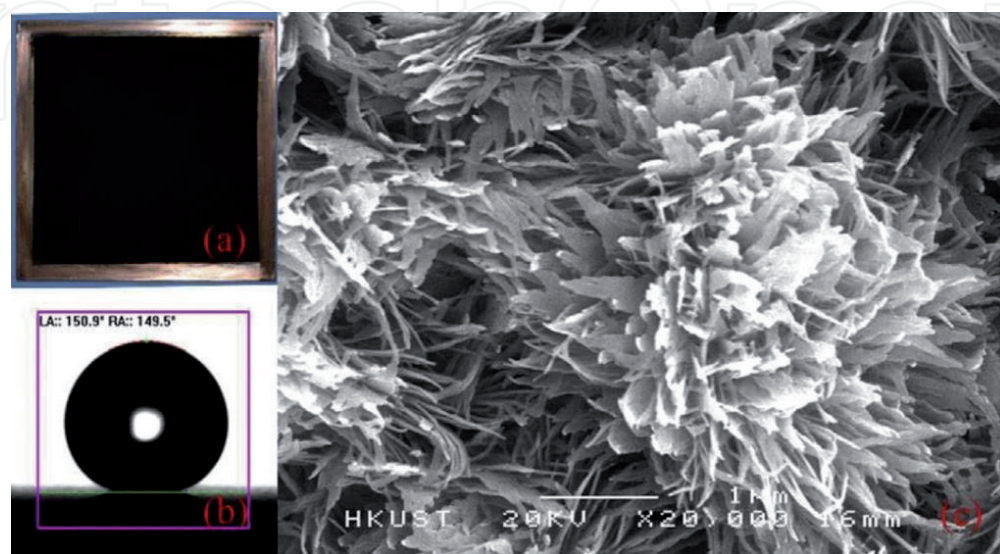


Figure 14. Features of the condenser: (a) front view of the condenser; (b) water contact angle of the condenser; and (c) amplified view of the nanostructure [26].

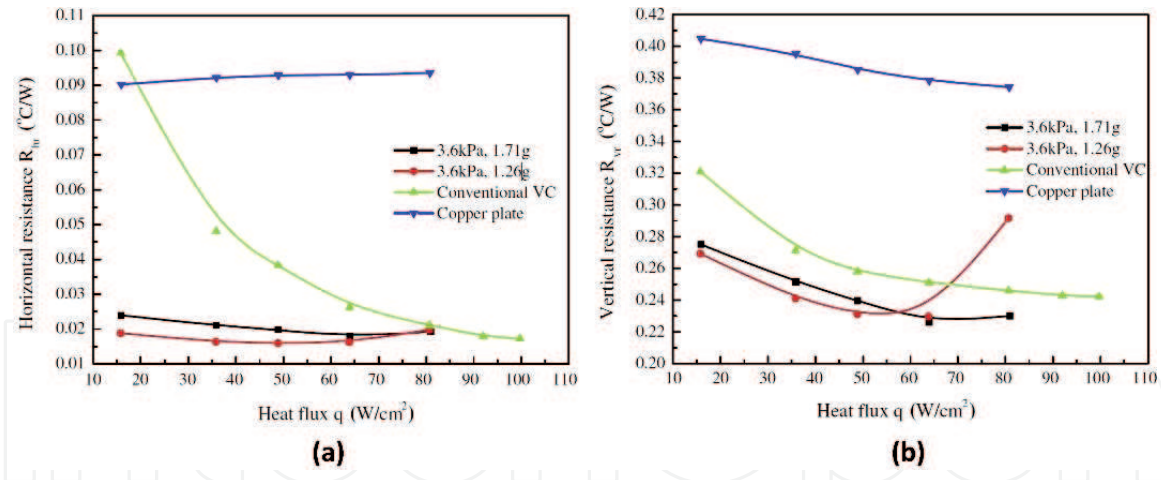


Figure 15.

Thermal performance comparison of the vapor chamber with a conventional vapor chamber and copper plate: (a) horizontal thermal resistance and (b) vertical thermal resistance [26].

1.71 g and 1.26 g. The pressure inside the vapor chamber is evacuated to 3.6 kPa. The conventional vapor chamber refers to a vapor chamber with symmetrical structure, which consists of two layers of copper mesh with 40 μm and 80 μm wire diameter sintered on both the evaporator and the condenser as a wick structure. Therefore, the evaporator and the condenser have the same hydrophilicity feature. The copper plate is a solid pure T2 copper solid heat spreader. The conventional vapor chamber and the copper plate have the same dimension as the asymmetric vapor chamber.

The asymmetric vapor chamber shows a much lower horizontal thermal resistance compared with the conventional vapor chamber and copper plate, as shown in **Figure 15(a)**. The horizontal thermal resistance of the asymmetric one is kept at around 0.02°C/W for all the testing heat flux. Especially, the horizontal thermal resistance at 15 W/cm² heat flux for the asymmetric one is only 1/5 of that for the conventional one which has a vertical thermal resistance even higher than that for the copper plate. The difference of the horizontal decreases with the increase of the heat flux and is eliminated at the heat flux of 82 W/cm². This proves that a nanostructured superhydrophobic condenser can enhance the temperature uniformity of the vapor chamber.

Figure 15(b) presents the vertical thermal resistance of different heat spreaders. Both types of the vapor chamber have a lower thermal resistance compared with the copper plate. Besides, the thermal resistance of the asymmetric one when the heat flux is less than 70 W/cm² is lower than that of the conventional one. However, when the heat flux is larger than 70 W/cm², the asymmetric one with 1.26 g water has a larger thermal resistance than that of the conventional one. This can be explained by insufficient water flowing back to the evaporator. Thus, increasing the amount of water may lower the vertical thermal resistance at the high heat flux for the asymmetric one, which is proved by the asymmetric one with 1.71 g shows a best vertical thermal performance at the heat flux of 82 W/cm².

In summary, the asymmetric vapor chamber with a nanostructured superhydrophobic condenser has a better thermal performance both in horizontal and vertical aspects when compared with the conventional vapor chamber. This can be explained as follows: the mode of the condensation on the condenser of the conventional vapor chamber is filmwise condensation which occurs at the hydrophilic surfaces while dropwise condensation is the mode for the condensation on the condenser of the asymmetric vapor chamber. Dropwise condensation has at least 3 times the heat transfer rate of filmwise condensation [25]. Thus, the thermal resistance of the condenser for the asymmetric vapor chamber is lower than that for the conventional one. Besides, droplets formed during dropwise condensation

can return to the evaporator by directly contacting or falling into the evaporator surface, while liquid film formed during filmwise condensation only can return the evaporator through the wick structure. Therefore, dropwise condensation induced by the nanostructured superhydrophobic surface also improves the backflow ability of the wick structure. As a result, a larger amount of heat is removed and spread to the whole inner space in the asymmetric vapor chamber.

The authors presented wettability modification and patterning can enhance the thermal performance of vapor chambers in this and the last sections. In the next section, another surface modification method, which is growing nanostructured on the microstructure to form a multiscale micro/nanostructured wick structure, also can improve the thermal performance of vapor chambers.

5. Multiscale micro/nanostructured wick structure for two-phase heat spreaders

Sintering a porous microstructure on the inner surface of the vapor chamber to form a wick structure is the most common way in the fabrication of a vapor chamber. Researchers tried to use various kinds of porous microstructure to enhance the thermal performance of the vapor chamber, while little research was focused on growing a nanostructure on the porous microstructure to form a multiscale micro/nanostructured wick structure for enhancing the thermal performance before 2010. However, the nanostructure can enlarge the area of thin-film evaporation, increase the nucleation sites for boiling and improve the backflow ability of the wick structure without changing the microstructure [27, 28]. Thus, the authors investigated the effect of the multiscale micro/nanostructured wick structure on several types of two-phase heat spreaders.

5.1 Fabrication and the test of the multiscale micro/nanostructured wick structure

The wick structure of the asymmetric vapor chamber with a nanostructured superhydrophobic condenser, which is described in the previous section, is nanostructured by a chemical surface modification method presented in Section 3.1. The bare sintered wick structure shown in **Figure 16(a)** is coated with a layer of a thin-film array of copper oxide, which is shown in **Figure 16(b)** and **(c)**. The thermal performance of the vapor chamber with a bare sintered wick structure is compared with that with a multiscale micro/nanostructured wick structure. The experimental setup is the same as described in Section 4.1. The uncertainties of vertical and horizontal thermal resistance for these vapor chambers are 0.7% and 0.8%, respectively.

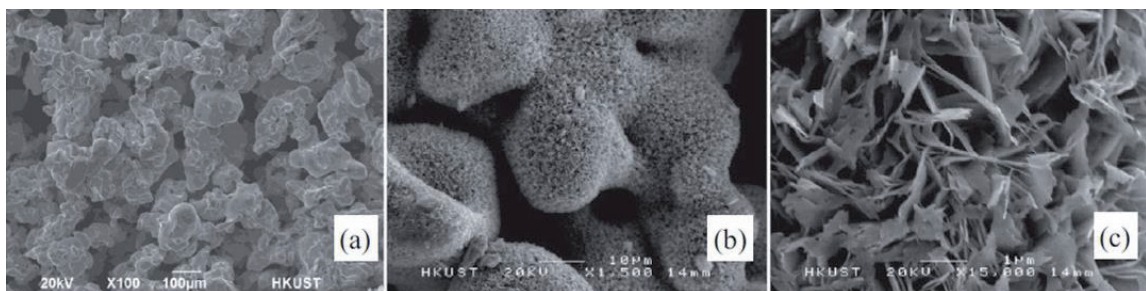


Figure 16. Scanning electron microscope (SEM) images of the wick structures of the asymmetric vapor chamber with a nanostructured superhydrophobic condenser: (a) bare sintered powder wick structure; (b) low-magnification of multiscale micro/nanostructured wick structure; and (c) high-magnification of multiscale micro/nanostructured wick structure [29].

Moreover, the thermal performance of the ultrathin vapor chamber case 1, which only has a copper-covered stainless-steel mesh wick structure (shown in **Figure 9(a)**), is compared with that of vapor chamber case 2, which has a multi-scale micro/nanostructured wick structure (shown in **Figure 9(b)**). The fabrications of other parts of these two types of vapor chambers can be found in sections 3.1 and 4.1. The parameters for assessing the thermal performance can be found in sections 3.2 and 4.1.

5.2 Effect of the multiscale micro/nanostructured wick structure on the thermal performance of two-phase heat spreaders

The thermal performance of two types of the asymmetric vapor chamber with different wick structures on the evaporator is compared with each other, as shown in **Figure 17**. The vertical thermal resistance for both vapor chambers decreases from around $0.63^\circ\text{C}/\text{W}$ to $0.32^\circ\text{C}/\text{W}$ when the heat flux increases from $5 \text{ W}/\text{cm}^2$ to the maximum test heat flux, which is shown in **Figure 17(a)**. However, the micro/nanostructured wick structure gives a quicker decrease of the vapor chamber at the low heat flux range compared with the bare sintered wick. For example, the vertical thermal resistance of the vapor chamber with micro/nanostructured wick shows a $0.25^\circ\text{C}/\text{W}$ decrement with the increase of the heat flux from $5 \text{ W}/\text{cm}^2$ to $35 \text{ W}/\text{cm}^2$. While with the bare sintered wick, it only decreases $0.18^\circ\text{C}/\text{W}$. Besides, the micro/nanostructured wick structure enhances the vertical thermal performance for all the test heat flux compared with the bare sintered wick. These can be explained as follows: In the low heat flux range, thin-film evaporation is the dominant heat transfer mode for the evaporator. The thin-fin array nanostructure grown on the microstructure surface increase the superficial area of the wick structure, leading to an enlargement of the thin-film evaporation area. Thus, the heat transfer rate of the evaporator is improved. In the high heat flux range, nucleate boiling replaces the thin-film evaporation to become the dominant heat transfer mode in the evaporator. As shown in **Figure 16(b)**, the nanostructure roughens the wick structure when compared with the bare sintered wick shown in **Figure 16(a)**, resulting in more nucleation sites in the wick structure. Thus, the extent of boiling in the evaporator is enhanced and the heat transfer rate is increased. Moreover, the backflow ability of the multiscale micro/nanostructured wick structure is enhanced owing to its super hydrophilicity. Thus, the vapor chamber can work well at high heat flux conditions.

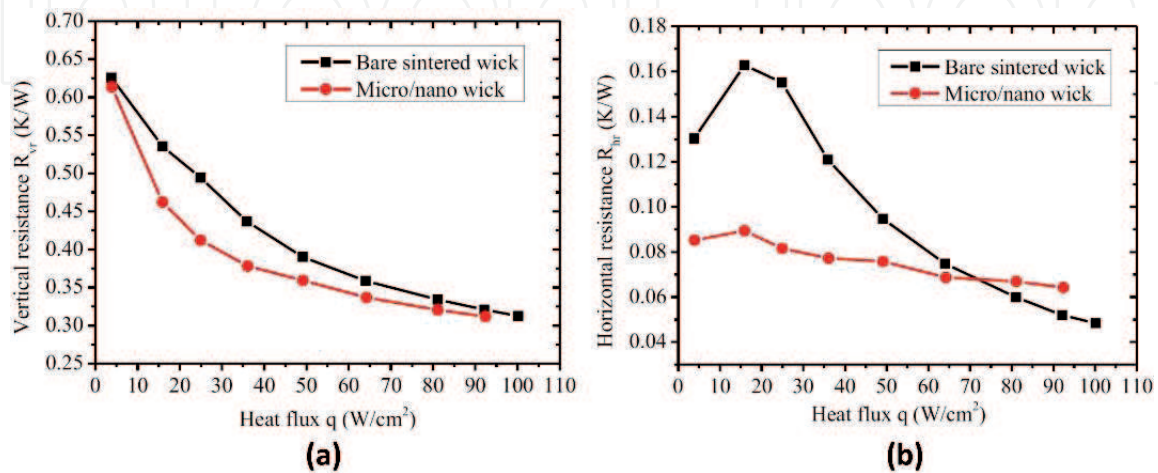


Figure 17.

Thermal performance comparison of the vapor chambers with different wick structures: (a) vertical thermal resistance and (b) horizontal thermal resistance [29].

The enhancement of the horizontal thermal performance, presented in **Figure 17(b)**, can be also explained with the advantages provided by the nanostructure. The improved thin-film evaporation at the low heat flux on the micro/nanostructured wick structure increases the amount of the vaporized liquid spreading to the whole space of the vapor chamber, resulting in a reduction of the horizontal thermal resistance by 30–50% within the heat flux ranging from 5 W/cm² to 35 W/cm². Besides, the micro/nanostructured wick structure gives a more stable horizontal thermal performance from low heat flux region to high heat flux region. Generally, the vapor chamber with a multiscale micro/nanostructured wick structure has a better horizontal thermal performance than that with a bare sintered wick structure.

The thermal performance of the ultrathin vapor chamber can be also enhanced by nanostructuring the wick structure to form a micro/nanostructured wick structure. As shown in **Figure 12(a)** and **(c)**, the difference of the horizontal thermal resistance between case 1 and case 2 under the optimum charge ratio (62.8% for case 1 and 60.4% for case 2) can be neglected within the range of heat flux from 8.59 W/cm² to 19.84 W/cm². However, it becomes obvious when the heat flux increases to 23.91 W/cm² owing to the occurrence of serious partial dry-out on the evaporator of case 2. A large increment of the vertical thermal resistance for case 1 is also found at the heat flux of 23.91 W/cm² while it for case 2 just slightly increases, which are shown in **Figure 12(b)** and **(d)**. These also prove the enhancement of the backflow ability induced by the multiscale wick. Besides, the vertical thermal resistance under the optimum charge ratio for case 2 is smaller than that for case 1 due to the enhancement of the thin-film evaporation that happened on the evaporator.

The authors also adopted the micro/nanostructured wick structure for another type of two-phase heat spreaders, the thermal ground plane, which works in a one-dimensional way [30]. By combining a two-layer structure with the multiscale wick, the thermal performance of the thermal ground plane is enhanced. Therefore, growing nanostructure on the microstructure surface to form a multiscale wick is an efficient way to improve the thermal performance of various kinds of two-phase heat spreaders.

6. Conclusion

In this chapter, several surface modification methods for improving the thermal performance of a two-phase heat spreader are introduced and discussed. Forming a wettability pattern on a surface enhances the evaporation of a droplet by elongating the length of the contact line. Thus, integrating the wettability pattern to the evaporator of a two-phase heat spreader is probably to enhance the thermal performance of the heat spreader, which is proved by the temperature uniformity enhancement of an ultrathin vapor chamber utilizing an evaporator with a wettability patterned surface. Changing the wettability of the condenser to superhydrophobic can also enhance the thermal performance by modifying the condensation mode from filmwise condensation to dropwise condensation which shows at least 3 times the heat transfer rate of the previous mode. Nanostructuring the microstructure to form a multiscale micro/nanostructured wick structure is also an efficient way to enhance the thermal performance of a two-phase heat spreader. It not only enhances the heat transfer rate on the evaporator but also increases the backflow ability of the wick structure, greatly improving the overall thermal performance of a two-phase heat spreader.

Acknowledgements

These works were supported by the Research Grants Council and Innovation Technology Commission (ITC) of the Government of Hong Kong Special Administrative Region (HKSAR) with RGC/GRF Project No. 617812, 16205018, 618210, ITS/530/09, and ITS/162/16FP, and the International Science and Technology Project of Huangpu District of Guangzhou City (2019GH02). We acknowledge assistance from the Nanosystem Fabrication Facility (NFF) of HKUST for the device/system fabrication.

Appendices and nomenclature

A_h	heater area
c_v	saturated water vapor concentration
d	hydrophobic island side length
D	vapor diffusivity
H	relative humidity
j	mass flux of evaporating flux
j_0	factor of mass flux vapor
k_{Cu}	thermal conductivity of copper
K_{eff}	in-plane effective thermal conductivity
l	distance from the heater to the center of the evaporator outside surface
m	evaporation rate
P	pitch distance of the hydrophobic islands
q	input heat flux
Q	input power
r_s	droplet radius
R	droplet contact line radius
R_{hr}	horizontal thermal resistance
R_{vr}	vertical thermal resistance
$R_{hr,Cu}$	measured horizontal thermal resistance of copper
$R_{hr,vc}$	measured horizontal thermal resistance of a vapor chamber
t	evaporation time from the beginning of the experiment
T	temperature
V_{water}	volume of water inside the ultrathin vapor chamber
V_{total}	total volume of the inner space for the ultrathin vapor chamber
x	length from a droplet center to the position
η	charge ratio of the ultrathin vapor chamber
θ	instant contact angle during the evaporation
π	Pi

IntechOpen

IntechOpen

Author details

Huihe Qiu* and Yinchuang Yang
The Hong Kong University of Science and Technology, Hong Kong SAR, China

*Address all correspondence to: meqiu@ust.hk

IntechOpen

© 2021 The Author(s). Licensee IntechOpen. This chapter is distributed under the terms of the Creative Commons Attribution License (<http://creativecommons.org/licenses/by/3.0>), which permits unrestricted use, distribution, and reproduction in any medium, provided the original work is properly cited. 

References

- [1] Ding C, Soni G, Bozorgi P, Piorek BD, Meinhart CD, MacDonald NC. A flat heat pipe architecture based on nanostructured titania. *Journal of Microelectromechanical Systems*. 2010;**19**(4):878-184
- [2] Oshman C, Shi B, Li C, Yang R, Lee YC, Peterson GP, et al. The development of polymer-based flat heat pipes. *Journal of Microelectromechanical Systems*. 2011;**20**(2):410-417
- [3] Oshman C, Li Q, Liew L-A, Yang R, Bright VM, Lee YC. Flat flexible polymer heat pipes. *Journal of Micromechanics and Microengineering*. 2013;**23**(1):015001
- [4] Chen Y-T, Kang S-W, Hung Y-H, Huang C-H, Chien K-C. Feasibility study of an aluminum vapor chamber with radial grooved and sintered powders wick structures. *Applied Thermal Engineering*. 2013;**51**(1-2):864-870
- [5] Chang C, Han Z, He X, Wang Z, Ji Y. 3D printed aluminum flat heat pipes with micro grooves for efficient thermal management of high power LEDs. *Scientific Reports*. 2021;**11**(1):8255
- [6] Li Y, Zhou W, He J, Yan Y, Li B, Zeng Z. Thermal performance of ultra-thin flattened heat pipes with composite wick structure. *Applied Thermal Engineering*. 2016;**102**:487-499
- [7] Li Y, He J, He H, Yan Y, Zeng Z, Li B. Investigation of ultra-thin flattened heat pipes with sintered wick structure. *Applied Thermal Engineering*. 2015;**86**:106-118
- [8] Lewis R, Xu S, Liew L-A, Coolidge C, Yang R, Lee Y-C. Thin flexible thermal ground planes: Fabrication and scaling characterization. *Journal of Microelectromechanical Systems*. 2015;**24**(6):2040-2048
- [9] Xu S, Lewis RJ, Liew L-A, Lee Y-C, Yang R. Development of ultra-thin thermal ground planes by using stainless-steel mesh as wicking structure. *Journal of Microelectromechanical Systems*. 2016;**25**(5):842-844
- [10] Huang G, Liu W, Luo Y, Li Y. A novel ultra-thin vapor chamber for heat dissipation in ultra-thin portable electronic devices. *Applied Thermal Engineering*. 2019;**114**:726
- [11] Tang Y, Tang H, Li J, Zhang S, Zhuang B, Sun Y. Experimental investigation of capillary force in a novel sintered copper mesh wick for ultra-thin heat pipes. *Applied Thermal Engineering*. 2017;**115**:1020-1030
- [12] Wan R, Wang C, Lei X, Zhou G, Fang H. Enhancement of water evaporation on solid surfaces with nanoscale hydrophobic-hydrophilic patterns. *Physical Review Letters*. 2015;**115**(19):195901
- [13] He M. Evaporation of multi-component droplets on homogeneous and heterogeneous wettability surfaces [Thesis]. Hong Kong: The Hong Kong University of Science and Technology; 2017
- [14] He M, Liao D, Qiu H. Multicomponent droplet evaporation on chemical micro-patterned surfaces. *Scientific Reports*. 2017;**7**:41897
- [15] Birdi KS, Vu DT. Wettability and the evaporation rates of fluids from solid surfaces. *Journal of Adhesion Science and Technology*. 1993;**7**(6):485-493
- [16] Ristenpart WD, Kim PG, Domingues C, Wan J, Stone HA. Influence of substrate conductivity on circulation reversal in evaporating drops. *Physical Review Letters*. 2007;**99**(23):234502
- [17] Hu H, Larson RG. Evaporation of a sessile droplet on a substrate.

The Journal of Physical Chemistry B.
2002;**106**(6):1334-1344

[18] Wang H, Garimella SV, Murthy JY. Characteristics of an evaporating thin film in a microchannel. *International Journal of Heat and Mass Transfer*. 2007;**50**(19-20):3933-3942

[19] Wang H, Garimella SV, Murthy JY. An analytical solution for the total heat transfer in the thin-film region of an evaporating meniscus. *International Journal of Heat and Mass Transfer*. 2008;**51**(25-26):6317-6322

[20] Ranjan R, Murthy JY, Garimella SV. Analysis of the wicking and thin-film evaporation characteristics of microstructures. *Journal of Heat Transfer*. 2009;**131**(10)

[21] Ranjan R, Murthy JY, Garimella SV. A microscale model for thin-film evaporation in capillary wick structures. *International Journal of Heat and Mass Transfer*. 2011;**54**(1-3):169-179

[22] Yang Y, Li J, Wang H, Liao D, Qiu H. Microstructured wettability pattern for enhancing thermal performance in an ultrathin vapor chamber. *Case Studies in Thermal Engineering*. 2021;**25**:100906

[23] Zhang X, Guo Y-G, Liu W-M, Hao J-C. CuO three-dimensional flowerlike nanostructures: Controlled synthesis and characterization. *Journal of Applied Physics*. 2008;**103**(11):114304

[24] Sugimura H, Hozumi A, Kameyama T, Takai O. Organosilane self-assembled monolayers formed at the vapour/solid interface. *Surface and Interface Analysis*. 2002;**34**(1):550-554

[25] Vemuri S, Kim KJ. An experimental and theoretical study on the concept of dropwise condensation. *International Journal of Heat and Mass Transfer*. 2006;**49**(3-4):649-657

[26] Sun Z, Chen X, Qiu H. Experimental investigation of a novel asymmetric heat

spreader with nanostructure surfaces. *Experimental Thermal and Fluid Science*. 2014;**52**:197-204

[27] Weibel JA, Kim SS, Fisher TS, Garimella SV. Carbon nanotube coatings for enhanced capillary-fed boiling from porous microstructures. *Nanoscale and Microscale Thermophysical Engineering*. 2012;**16**(1):1-17

[28] Ranjan R, Garimella SV, Murthy JY, Yazawa K. Assessment of nanostructured capillary wicks for passive two-phase heat transport. *Nanoscale and Microscale Thermophysical Engineering*. 2011;**15**(3):179-194

[29] Sun Z, Qiu H. An asymmetrical vapor chamber with multiscale micro/nanostructured surfaces. *International Communications in Heat and Mass Transfer*. 2014;**58**:40-44

[30] Yang Y, Liao D, Wang H, Qu J, Li J, Qiu H. Development of ultrathin thermal ground plane with multiscale micro/nanostructured wicks. *Case Studies in Thermal Engineering*. 2020;**100738**